RSC Advances

PAPER

View Article Online
View Journal | View Issue

Cite this: *RSC Adv.*, 2021, **11**, 36125

Biomass derived hierarchical porous carbon for high-performance O_2/N_2 adsorption; a new green self-activation approach

Hossein Mashhadimoslem,[a] Mobin Safarzadeh,[b] Ahad Ghaemi,[*a] Hosein Banna Motejadded Emrooz*[b] and Masoud Barzegar[b]

Biomass-derived porous carbons are the most common adsorbent materials for O_2/N_2 adsorption because of their excellent textural properties, high surface area, and low expense. A new synthesis method based on a self-activation technique was developed for a new green porous carbon adsorbent. This ecofriendly system was used for the synthesis of hierarchical porous carbons from walnut-shell precursors. The sorbent was successfully synthesized by facile one-step carbonization, with the activating reagents being gases released during the activation. The sample morphology and structure were characterized by field emission scanning electron microscopy, high-resolution transmission electron microscopy, Raman, Fourier transform infrared spectra, X-ray photoelectron spectroscopy, X-ray powder diffraction, thermogravimetric, and differential thermal analysis. The optimal porous carbons were synthesized at 1000 °C, providing a surface area as high as 2042.4 (m^2 g^{-1}) and micropore volume of about 0.499 (m^3 g^{-1}). At 298 °K under 9.5 bar pressure, the potential for O_2/N_2 separation using porous carbon samples was studied, and the sips isotherms with the highest adsorption potential were determined to be 2.94 (mmol g^{-1}) and 2.67 (mmol g^{-1}), respectively. The sample exhibited stable O_2/N_2 separation over ten cycles, showing high reusability for air separation. Finally, the technology described presents a promising strategy for producing eco-friendly porous carbon from a variety of biomass on an industrial scale.

Received 9th September 2021
Accepted 28th October 2021

DOI: 10.1039/d1ra06781h

rsc.li/rsc-advances

1 Introduction

Gas separation process technologies play an influential role in various industries including medical, food, chemical, petrochemical, and power generation industries.[1,2] Pressure swing adsorption (PSA) is one of the most cost-effective solutions for air separation applications in response to industrial requirements for nitrogen and oxygen processing.[3,4] In the 1950s, air separation systems based on a pressure swing were established.[5] One of the special applications of air separation technology in the power plant industry is oxyfuel, which is one of the solutions to reduce carbon dioxide.[6,7] The PSA technology is a cyclic adsorption process in gas separation using different adsorbents and adsorption capacity rates.[8,9] Molecular adsorbents are used to separate and purify various gas species from a gas mixture under pressure using the PSA technique. This process usually operates at low pressure and ambient temperatures.[2,10] Various adsorbents such as porous carbon, zeolites, carbon molecular baskets (CMB), and carbon molecular sieves (CMS) are used to adsorb the subject gas molecules at pressure swing.[11]

2 Literature review

For air separation, both physisorption and chemisorption processes are utilized, but the physisorption mechanism has become more common due to the low bond energy between gas and solid adsorbent, as well as the low-cost energy of sorbent regeneration.[11,12] Recently, various physisorption-adsorbent such as zeolites are used in the O_2/N_2 adsorption as porous crystalline aluminosilicates.[13] They have open crystal lattices that contain pores of molecular size, and gas molecules can diffuse them. The selective gas separation by zeolites requires control of the structure and composition of the framework, shape, and distribution of cations within the cavities.[14] The breathtaking adsorption of zeolites for air separation is used in the continuous development of nitrogen adsorbents from the air. At room temperature, the ability of zeolites to separate air has revealed that nitrogen uptake capacity is greater than oxygen adsorption capacity.[15,16] Metal–organic frameworks (MOFs) are composed of organic ligands or "struts" coordinated to metal-based nodes to form a three-dimensional extended network.[17] Much research has been done on the MOFs with tunable pore size, high surface area, ability to functionalize the

[a]*School of Chemical, Petroleum and Gas Engineering, Iran University of Science and Technology (IUST), Narmak, 16846, Tehran, Iran. E-mail: aghaemi@iust.ac.ir*

[b]*Nanotechnology Department, School of Advanced Technologies, Iran University of Science and Technology (IUST), Narmak, 16846, Tehran, Iran. E-mail: Motejadded@iust.ac.ir; Tel: +98 21 77240496*

walls of cavities, and particularly, open metal sites for gas separation and storage.[17–24] Experiments at high pressures and extremely low temperatures have been reported, therefore these points impose operational constraints. Carbon-based adsorbents are suitable for gas adsorption and are divided into different categories based on morphology, porosity, and structure, such as carbon nanotubes, graphene, and fullerenes.[18,25–29] Despite their high adsorption efficiency, these adsorbents have drawbacks such as high synthesis costs, environmental impacts, and the use of toxic chemicals during synthesis.[22,23] Porous carbon, unlike carbon-based adsorbents, does not have the aforementioned drawbacks.

Porous carbon has a wide range of uses, including catalysts, heavy metals adsorbents, separation of various gases, energy storage, and electrochemical materials, due to its unique characteristics.[30] The porous carbon media is structurally complex and the total volume, size, and distribution of the pores determine how the molecules of a gas are adsorbed on the porous carbon, which these pores have strong van der Waals forces for the adsorption process.[31] Natural precursors biomass can be used for porous carbon synthesis such as rice straw, tobacco, coffee, pine cone, palm shell, *etc.* due to renewable, cost-effective, and eco-friendly.[32–34] The broad range, the abundance of nature, and the renewability of precursors used in the synthesis process distinguish porous carbon fabrication from that of other sorbents.[35] Since biomass-derived porous carbon has a large surface area (up to 3072 $m^2\ g^{-1}$), its density and morphology are influenced by the synthesis process.[36] In recent years the traditional methods such as chemical and physical activation have commonly been used to activate/pyrolyze a variety of carbonaceous biomass. Porous carbons can be pyrolyzed/activated by physical (with CO_2, N_2, steam, O_2, and NH_3) or chemical (H_3PO_4, HCl, KOH, NaOH, and $ZnCl_2$) activation of the carbon precursors that may occur in a one or two-steps process.[37,38] The type of precursor, activating agent, activation temperature, and the ratio of activating agent to precursor are the key parameters that impact porosity composition, pore size distribution, and pore volume.[29,39,40] The synthesis and carbonization method to prepare porous carbon is one of the influential features in the characteristics of porous carbon materials.[41] In the physical activation method, the mentioned gases are used at a temperature below 1000 °C, while in the chemical activation method, acidic and alkaline agents are used to impregnate.[42] Chemical activation is favored due to the resulting material's tendency to be mesoporous and tunable porosities, even though physical activation is less expensive and has a lesser environmental effect. Chemical activation, on the other side, is frequently afflicted by toxic gases released during pyrolysis, process complexity, and device corrosion, and is not environmentally friendly.[43–45]

The direct pyrolysis method is a step forward in the production of porous carbons since it removes the need for post-synthesis activation. A novel self-activation approach for porous carbon synthesis has been developed in recent years as a result of the aforementioned limitations. In recent research, intrinsic hydroxyapatites were employed as natural templates to produce N-doped mesopore-dominant carbon materials utilizing a one-step self-activation method under N_2 atmosphere. As discussed, this method is not considered self-activation due to the use of inert gases and templates during the process.[46–48]

The present work proposed a green, low-cost and facile method to prepare green porous carbon with mesopore-dominant from walnut-shell as precursors using a one-step self-activating system. The proposed approach is based on a closed-loop carbonization system that uses gases decomposition from biomass as the reagent. To better understand the role of the self-activating system, the pyrolysis process was performed with and without argon gas to determine the effect of this system on the structure. In the following, the present report proposed the high-performance green porous carbon adsorbent for O_2/N_2 adsorption. Adsorption equilibrium and kinetics experiments of O_2/N_2 were also performed to obtain the adsorption capacity and kinetics. The morphology and structure, as well as chemical constitution of the resulting porous carbon, were characterized by field emission scanning electron and high-resolution transmission electron microscopy, Raman and Fourier-transform infrared spectroscopy (FTIR), X-ray photoelectron spectroscopy (XPS), powder X-ray diffraction (XRD), thermogravimetry-differential thermal analysis (DTA-TG) and N_2 adsorption–desorption analysis, in which the influence of the treatment method on the morphology and porous texture of the material was also demonstrated. By use of a virtual representation of a large surface area (up to 2042.4 $m^2\ g^{-1}$) and availability, the resulting porous carbons show great potential as functional sorbents for gas storage and separation.

3 Experimental

3.1 Materials

In the current study, all chemicals and reagents were analytical grade and were utilized without additional purification as supplied. Walnut-shell biomass was collected from walnut trees on the campus area of Iran University and Science Technology (Tehran, Iran). This biomass was rinsed multiple times before being treated to eliminate visible impurities. Hydrochloric acid (37%) was purchased form was purchased from Dr Mojallali™ Company (Tehran, Iran), and, O_2 (99.999%), N_2 (99.999%), Ar (99.999%) were supplied by Arman Gas Company (Tehran, Iran).

3.2 Self-activating system for preparation of porous carbon

A sealed chamber, a tubular electric furnace, an air pump, and eventually a condenser are all part of the self-activating synthesis system that is connected by pipes. Both ends of the quartz tube were sealed with rubber. During the synthesis process, no gas is released into the atmosphere since the system is sealed. An aluminum combusting boat holding a specific amount of different types of biomass was put in the hot zone (up to 1373 K) during the pyrolysis process. With the assistance of an air pump positioned at the system, the gases produced throughout the pyrolysis of the feeding biomass are cycled in a closed-loop channel. With the help of these gases, the activation process is carried out. As a result, no further activating agent is required. A

condenser is also placed along the gas's path, collecting and converting a part of the exhaust gases to liquid.

To prepare activated carbon, walnut-shell powder was directly pyrolyzed in a tubular electric furnace with a quartz tube under an argon atmosphere and without it at 1000 °C (heating rate: 5 °C min^{-1}). The samples were held at the maximum temperature for 3 h. After cooling to room temperature, the obtained product was washed and stirred with 1 M HCl and ultrapure water to remove impurities. Ultimately, filtration was applied until neutral pH and the residue was thoroughly washed with deionized water and dried at 95 °C for 12 h. The corresponding products were identified as W1000 (self-activated after pickling in 1000 °C), W1000-B (self-activated before pickling), W1000-Ar (self-activated under argon, after pickling in 1000 °C), and W1000-Ar-B (self-activated under argon, before pickling in 1000 °C). Fig. 1 shows a schematic view of the self-activating used in the present study.

3.3 Characterization

Micromeritics ASAP2020 (US) adsorption analyzers was employed to measure the N_2 adsorption–desorption isotherms at 77 K. Before performing the adsorption–desorption analyses, samples were degassed under dynamic vacuum conditions to constant weight at a temperature of 150 °C for 6 h. FTIR spectroscopy was accomplished on a PerkinElmer Spectrometer in the range of 500–4000 cm^{-1} with KBr pallets. Raman spectroscopy was conducted on a Takram micro-Raman spectrometer (Teksan™, Iran). X-ray photoelectron spectroscopy (XPS) measurements were carried out on an Al Ka source (XPS Spectrometer Kratos AXIS Supra). High-resolution transmission electron micrographs were obtained on a 300 kV FEI (US) TITAN microscope (HR-TEM). Thermogravimetric and differential thermal analyses (DTA/TG) in argon and air atmosphere were conducted on a Q600 (US) TA. Field emission scanning electron microscopy (FESEM) was observed on a Nanosem 450 microscope.

3.4 O_2/N_2 Adsorption–desorption measurement

A fixed bed adsorption reactor was built as shown in Fig. 2 to test the adsorption/desorption capacity of sorbent using the volumetric approach. For experiments, pure O_2 and N_2 were used as a feed to study the adsorption capacity on the sorbent surface. Each experiment by 1 g sorbent was tested in a fixed bed reactor sealed of the experimental set-up. Before the start-up test, the N_2 gas purging at 380 °K for 30 min in the experimental set-up was used. The experimental tests were performed at 298, 308, 318, and 328 °K temperatures under pressures rating 2 to 9.5 bar for 60 min. Due to the mixing tank in the passage, the CO_2 pressure and temperature were stabilized, and the stable gas was then fed to the adsorbent reactor. The pressure difference recorded at fixed temperature using pressure-temperature sensors and computer panel during the time was used to assess the adsorption parameters. The electrical heat tracing for the temperature stabilizer was used.

4 Results and discussions

4.1 Characterization analysis

DTA/TG analysis method has been accomplished in argon and air atmospheres to reveal the stability of the precursor,

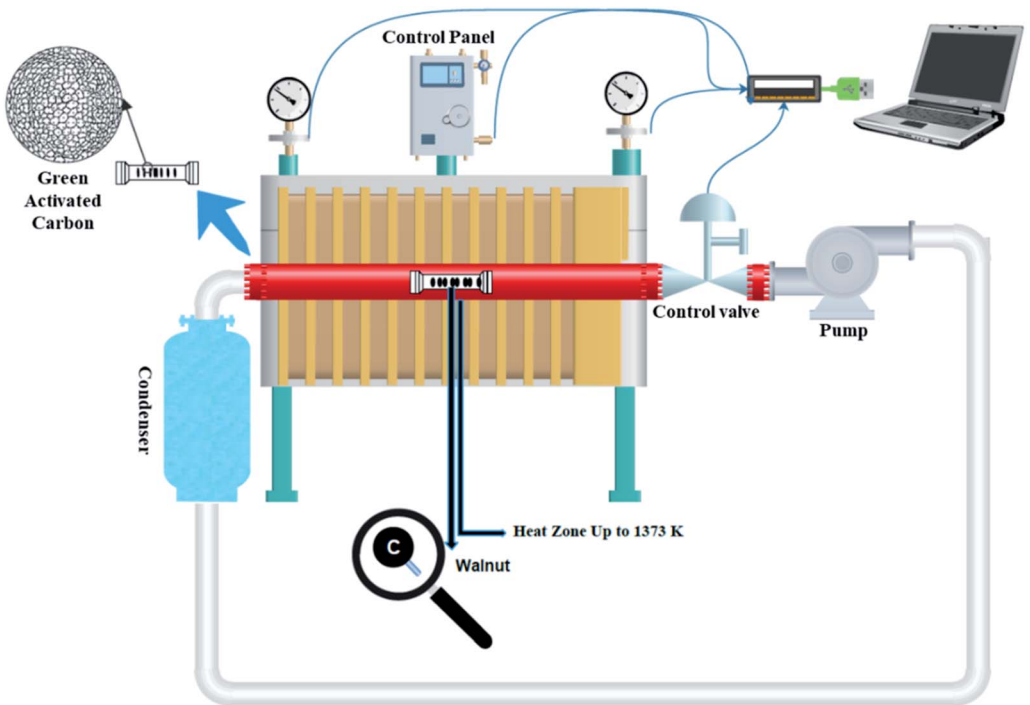

Fig. 1 Schematic of the self-activating synthesis setup.

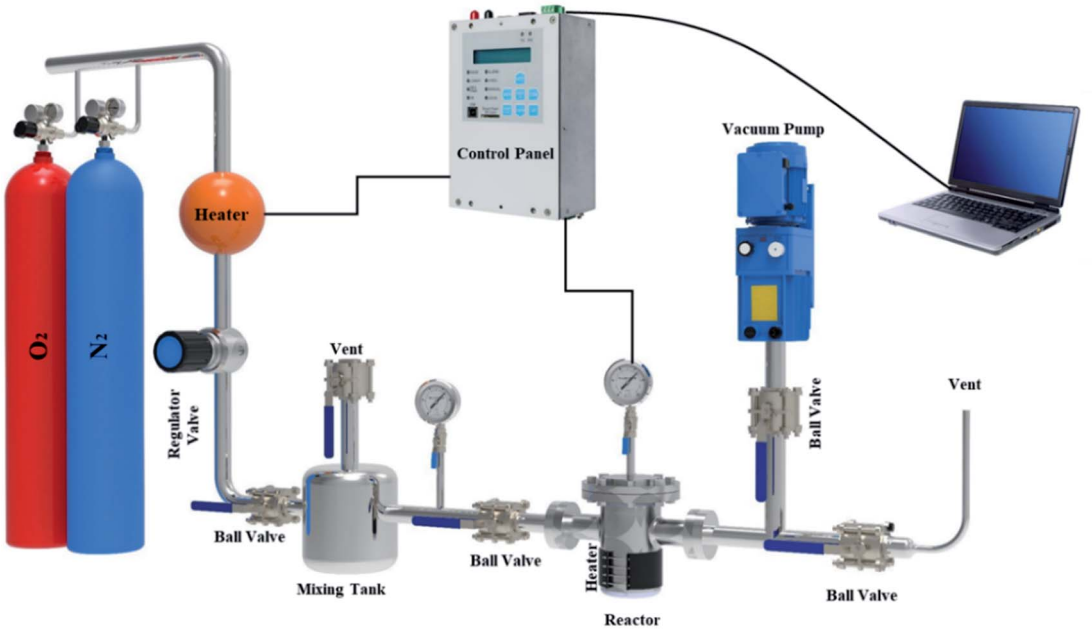

Fig. 2 The experimental set-up in the schematic view.

exothermic or endothermic reactions during pyrolysis, the amount of moisture and volatile matter lost from 50 °C to 1200 °C (Fig. 3).[12,44] As can be seen in Fig. 3(a and b), in the first step, both conditions' TG curves show a ~7.5–10.5% mass loss up to 200 °C due to the removal of adsorbed water molecules. Additionally, DTA curves show an endothermic reaction owing to the evaporation of moisture found in walnut-shell.[49] The next step begins at the first to the second turning point of the plots (220–400 °C for argon and 220–600 °C for air) has the highest weight loss, which represents the thermal elimination of organic components, hemicellulose, cellulose, and lignin. The third stage is the burning of lignin leftovers, which takes place at elevated temperatures. In the air atmosphere, the weight of the precursor decreases gradually with a temperature up to 580 °C. Conversely, the weight loss process decreases slightly above this temperature (580–850 °C) and reaches a steady pace at high temperatures due to oxygen consumption. In an argon atmosphere, weight loss is fast up to 380 °C, while at high temperatures is moderate. Moreover, DTA curves of both atmospheres show an exothermic reaction that represents the thermal decomposition of the walnut-shell.[49,50] As mentioned exothermic peaks, burning the precursor produces, confirm CO_2 production, indicating that walnut-shell combustion takes place in both atmospheres. This implies there is enough oxygen in the walnut-shell components for the combustion process to take place.[33]

The activation strength of the introduced self-activating system is demonstrated by the nitrogen adsorption–desorption analysis results of the pyrolyzed walnut-shell in Fig. 4. N_2 adsorption–desorption, micropores-plots (MP plot), and the

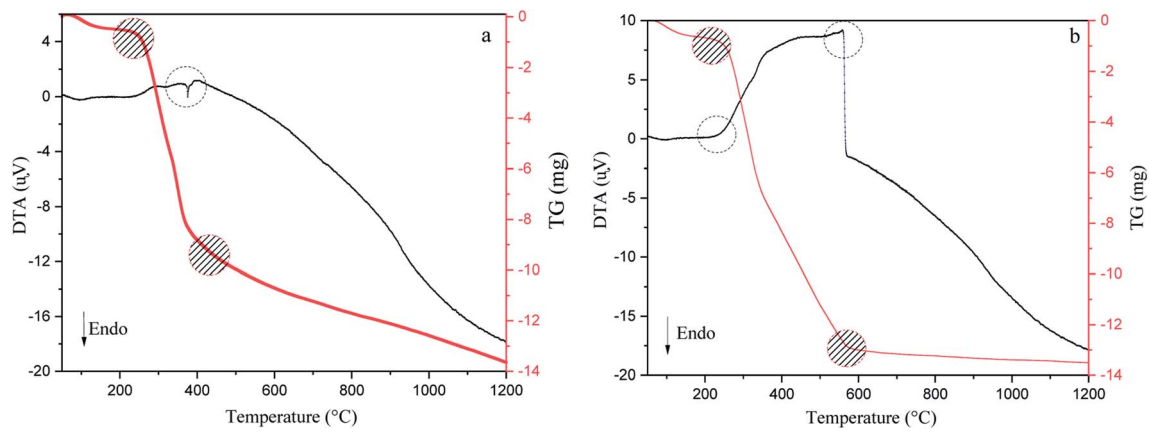

Fig. 3 Thermogravimetric and differential thermal analysis results of walnut-shell in argon (a) and air (b) atmosphere from 50 °C to 1200 °C.

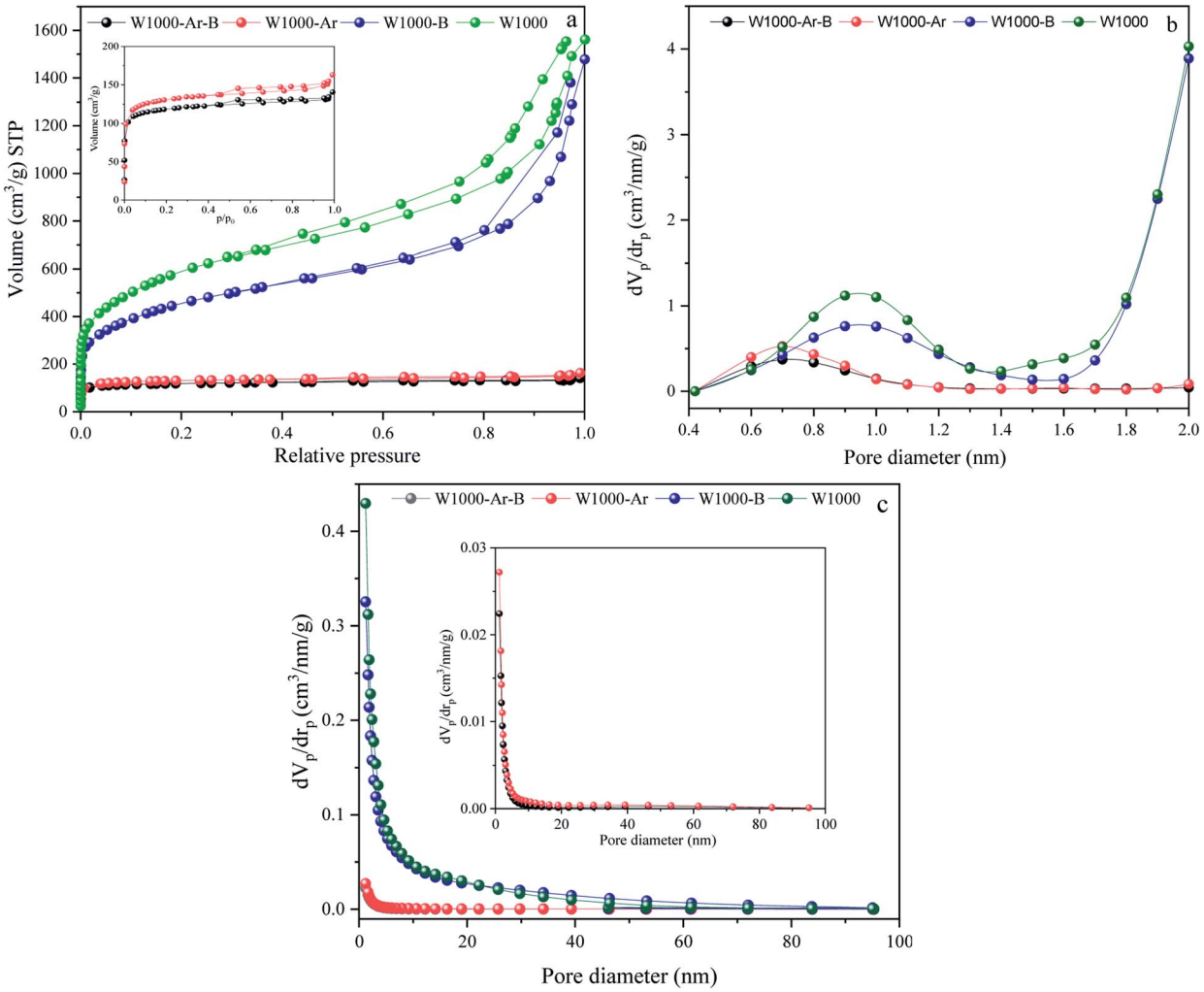

Fig. 4 N_2 adsorption/desorption isotherms, (a), MP plots (pores smaller than 2 nm) (b), and BJH pore size distributions curves (c) of porous carbons.

pore size distribution (PSD) of various green porous carbons can be seen in Fig. 4(a–c). Moreover, the detailed textural properties of green porous carbons can be observed in Table 1. The specific surface area, mean pore diameter and, total pore volume of the walnut-shell pyrolyzed under argon atmosphere are 488.2 m^2 g^{-1}, 2.05 nm, and 0.24 cm^3 g^{-1} which confirms that a self-activating system can form porous carbon under argon atmosphere. Conversely, the self-activating system without argon circulate the released gases such as CO_2, CO, H_2, and H_2O, which shows the increment of mesopore volumes as seen by the much higher N_2 adsorption. With the aid of this system, the specific surface area of W1000 has been greatly increased (2042.4 m^2 g^{-1}) compared to the W1000-Ar, which shows the capability of a self-activation synthesis system. The volume increased steadily at low relative pressure ($P/P_0 > 0.1$) in the N_2 sorption plot, indicating the presence of micropores.[51,52] The H_1-type hysteresis loop at $P/P_0 > 0.5$ for all samples is the capillary condensation phenomenon, showing the affluence meso–micro porous characteristics which confirm the results of the table. Based on MP plot results, W1000 has 0.83 cm^3 g^{-1} and

Table 1 Detailed textural properties of green porous carbons

Sample ID	Specific surface area (m^2 g^{-1})	Average pore diameter (nm)	Total pore volume (cm^3 g^{-1})	Mesoporous volume (cm^3 g^{-1})	Microporous volume (cm^3 g^{-1})
W1000-Ar-B	450.94	1.9241	0.24	0.2	0.04
W1000-Ar	488.21	2.0542	0.28	0.22	0.06
W1000-B	1580.1	5.4821	2.33	0.56	1.77
W1000	2042.4	4.6401	2.68	0.83	1.85

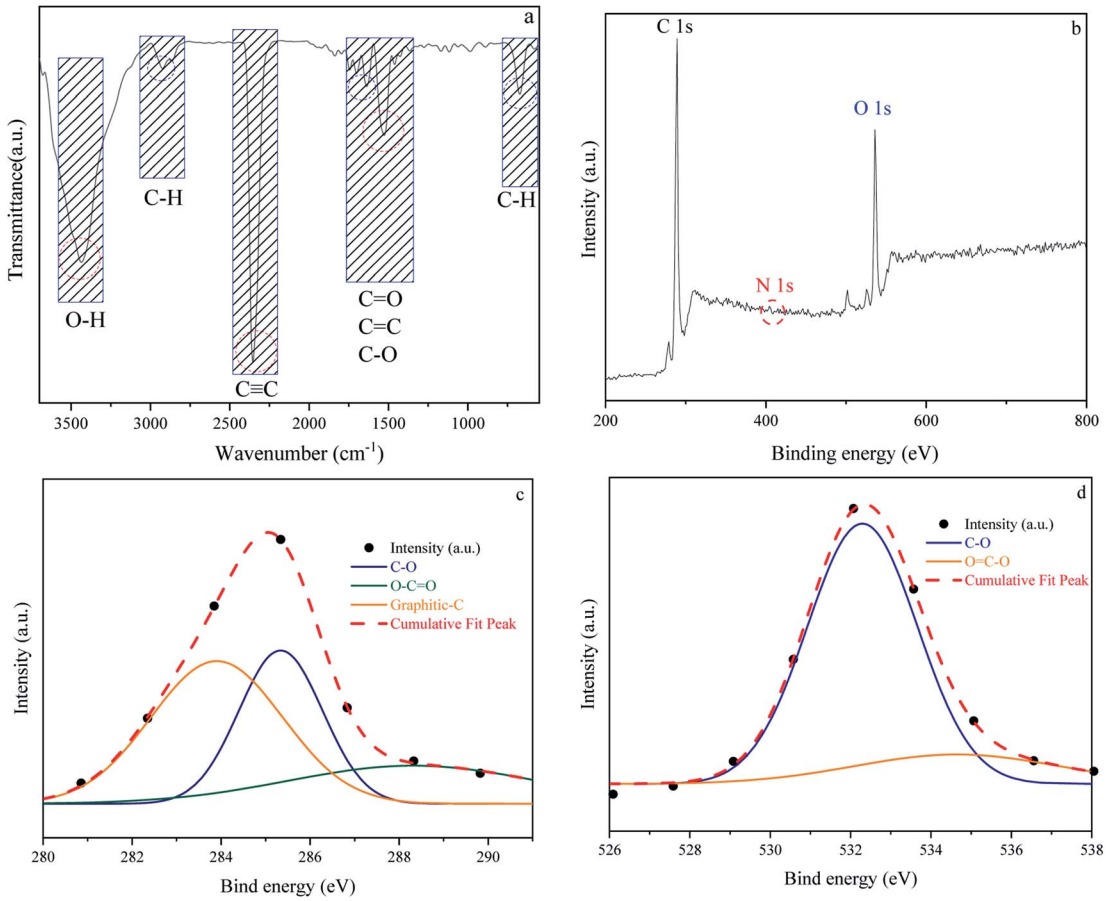

Fig. 5 Fourier transform infrared spectroscopy results of W1000 (a), XPS survey spectrum of W1000 showing the presence of C, N and O elements in the structure (b), C 1s (c) and O 1s (d), peak deconvolution.

1.85 $cm^3\ g^{-1}$ mesopores and micropores volume which is much larger than the sample synthesized under argon atmosphere. It shows that more elevated temperatures are favorable for micropore formation. The concurrent rise in micropore and mesopore volume indicates that new pore formation and pore widening occurred at the same time, and the production of micropores did not compromise the W1000 mesopore structure. The PSD presents the hierarchical porous structure of the self-activated instances, composed of micropores (0.5–2 nm), small mesopores (2–10 nm), and large mesopores/macropores (10–60 nm) with large size mesopores and abundant micropores.[53–55] As summarized in Table 1, the acid-pickled samples provide a larger specific surface area (488.21–2042.4 $m^2\ g^{-1}$) and a pore volume (0.28–2.68 $cm^3\ g^{-1}$) than the others, due to removing impurities during pickling. Pickling of porous carbon with acidic solutions (HCl) resulted in the removal of the inorganic compounds that mainly generate mesopore structures. By disappearing these compounds from the surface, voids appear, which firstly increase the volume of porosity and secondly increase the specific surface area.[56,57]

According to the results of the textural properties and DTA/TG, the general mechanism of self-activation can be achieved, which is expressed in the following reactions:

$$H_2O_{(l)} \rightarrow H_2O_{(g)} \quad (1)$$

$$C_{(s)} + H_2O_{(g)} \rightarrow CO_{(g)} + H_{2(g)} \quad (2)$$

$$2C_{(s)} + O_{2(g)} \rightarrow 2CO_{(g)} \quad (3)$$

$$CO_{(g)} + H_2O_{(g)} \rightarrow CO_{2(g)} + H_{2(g)} \quad (4)$$

$$C_{(s)} + CO_{2(g)} \rightarrow 2CO_{(g)} \quad (5)$$

At low temperatures, the moisture is gradually removed and converted to vapor. Activation begins slowly at temperatures above 700 °C, and the evolved H_2, H_2O, CO, and CO_2 gases during the pyrolysis process with continuous rotation in the circulatory system, carry out a key role in the self-activation process.[58–60] When the activation temperature increases (≥700 °C) the standard Gibbs free energy change of the Boudouard reaction (5) becomes negative. As a result, CO_2 and steam (H_2O), which are produced by the decomposition gases of cellulose, may react with carbon atoms and can penetrate into the interior of the carbon material to increase the porosity. Both the reactions of carbon with CO_2 and H_2O are endothermic which are consistent with the DTA results. Pyrolyzation at ≥850 °C is high enough to effectively initiate the reaction (4). As the activation temperature rises, the equilibrium constant decreases. This

indicates the Boudouard reaction is faster in favor of CO production and solid carbon consumption, as seen by the TG's weight loss. Through the Boudouard reaction, carbon atoms were separately stripped from their surfaces to create carbon monoxide and hydrogen in the gas phase. As well, as demonstrated in reaction (4), the exothermic water-gas shift reaction between steam and carbon monoxide may occur, resulting in CO_2 and H_2 as catalyzed by the carbon surface.[48,61,62] The pore-forming process in this system has two parts, with temperatures ranging from 200 to 600 °C and 650 to 1000 °C, respectively. Initially, the channel is created by a huge amount of pyrolysis gases escaping from biomass. Secondly, the pyrolysis gases were forced into the channel of char, causing the collapse of adjacent pores. It led to creating micro–meso pores by gasification reactions with carbon.[63,64]

In addition to carbon atoms, self-incorporated heteroatoms such as N- and/or O- dopants, which are typically components of the precursors' original structure, can improve the inherent characteristics of the porous carbon, resulting in enriched surface-active sites.[65–67] Furthermore, functional groups comprising the aforementioned heteroatoms can have a significant impact on the final product's behavior in a variety of applications, including gas adsorption. Acidity, electronegativity, and oxyfunctionalized molecules determine the surface chemistry of porous carbons.[68–70] Fig. 5 depicts the surface chemical properties of the W1000. As can be seen, the FTIR spectra of chemical bond vibration and specific functional groups have been shown in Fig. 5(a). The mentioned figure demonstrates a peak at approximately 3500 (cm^{-1}), which is typically assigned to O–H stretching vibration of hydroxyl bands. At lower wavenumbers, the location and asymmetry of this band suggest the presence of strong hydrogen bonding. The peak in the 2350 (cm^{-1}) range is related to R–C≡C–H bonds and assigns the presence of C≡C (alkynes) stretching vibration. Moreover, the band at 1732 (cm^{-1}) indicates the presence of the C=O vibration of the carbonyl group in acidic oxygen surface groups; the bands at 1500–1700 (cm^{-1}) display the C=C vibrations (alkenes) in the aromatic group. The bands at 1460–1350 (cm^{-1}) depict the C–O vibrations in the carboxylate group. Eventually, a weak bond at around 700 (cm^{-1}) is associated with the structure of aromatic C–H out-of-plane bending vibration (benzene ring).[68,71–74] Carboxyl functional bands show the weak intensity of peaks due to the high temperature of porous carbon synthesis. After activation at high temperature, the intensity of C=O was apparently decreased, implying that the carboxylic groups were converted to –OH groups. This confirms the role of steam in the self-activating system.[75,76]

The surface elemental composition and chemical bond configuration of W1000 were characterized by XPS measurement. In the survey spectrum carbon, oxygen and nitrogen can be identified by photoelectrons of their 1s orbitals. As shown in Fig. 5(b)–(d) as expected, the surface composition of the sample is composed of carbon species (68%) and a rich distribution of oxygen (31.4%) on the surface. Furthermore, N 1s (0.6%) peak can also be observed at around 401.5 eV on the surface. The C 1s (sp^3-boned) spectrum was deconvoluted into three peaks representing sp^2 hybridized graphitic-C (284 eV), phenolic C–O (285.9 eV), and O–C=O (288.1 eV) groups. O 1s spectrum was fitted by two peaks, located at 532 and 534 eV, which could be belonged to C–O and O=C–O groups.[43,58,77] The high temperature of the synthesis leads to an increase in the amount of oxygen and nitrogen increasingly disappear, which is consistent with the results of FTIR. These abundant oxygen functional groups on the surface of porous carbon couple with the high specific surface area offer a strong tendency to gas adsorption.[78,79]

The morphology and crystallinity of the W1000 have been demonstrated in Fig. 6. The development of porosity and changes in the surface morphology was shown by using a FESEM. As shown in Fig. 6(a)–(c), the sample revealed a cauliflower-like structure and a highly irregular porous. It can be seen rougher textures with heterogeneous surfaces and porous with many cavities. Furthermore, it can be seen that the size distribution of the pores, as critical factors determining its applicability, occurred randomly at the sample surface. When synthesis occurs with a gradual increase in temperature, cellulose is changed to porous solid carbon. These changes led to the opening of pores and the spaces between the crystallites. Owing to the thermal degradation of porous carbon occurring at high temperatures, the part of the micropores structure collapses and became mesoporous, confirming the results of BJH. Ultimately, the increase of the pore development in the ACs has a key role due to these pores acting as the active sites for gas adsorption, during the pyrolysis.[50,51,80–83]

The fabrication of the W1000 can be verified by the HRTEM images, showing the development of crystallinity and graphite plates of the porous structure. Fig. 6(d)–(f) illustrates the disordered carbon graphite layers with an approximate short-range lattice spacing (0.07 nm). As it can be seen, the sample consists of disordered mesostructured typical of amorphous carbon with some defects alongside low crystallization. Furthermore, Fig. 6(d) shows an interconnected hierarchical porous structure, including porosity with different dimensions of wormhole-like pores (meso–micro) which comprise large amounts of mesoporous.[36,84–86]

Raman spectroscopy analyses (Fig. 6(g)) were used to evaluate the degree of structural graphitization of the W1000. Raman spectra display two peaks at 1340 cm^{-1} (D band) and 1593 cm^{-1} (G band). D band is attributed to the double-resonance effect of disordered and defects in biomass-based porous carbon (sp^3-bond) and G band is ascribed to the in-plane stretching of sp^2-bond and graphite in-plane vibrations with E_{2g} symmetry. Moreover, the appearance of a 2D-band about 2700 cm^{-1} indicates a higher degree of graphitization and is linked to the association between graphite plates, which is the cause of graphite formation in the carbon structure.[87–89] The integral intensity ratio of D to G bands ($I_d/I_g = 1.36$) is higher than 1.00. This point indicated that a number of defects present on the carbon surface, poor graphitization, and the tendency of the structure to be amorphous as to be seen in HRTEM Fig. 6(e) and (f). Although higher temperatures usually cause graphite to increase, sometimes destroys the graphite structure, which can be a reason for the irregularity of the synthesized sample at 1000 °C.[87,90]

As can be observed in Fig. 6(h), X-ray diffraction patterns clearly show the development of turbostratic carbon with structural ordering intermediate between amorphous carbon

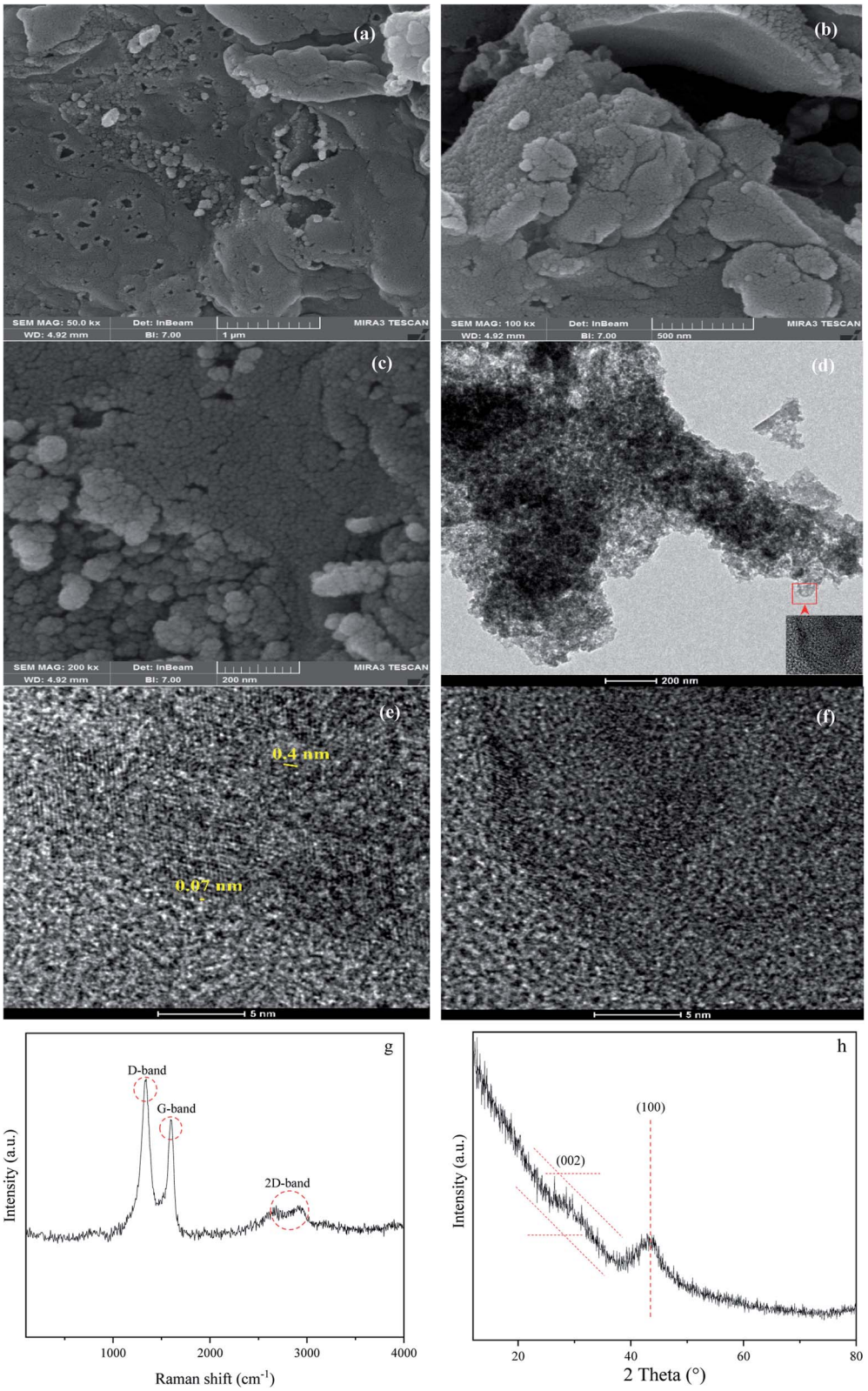

Fig. 6 FESEM micrographs showing cauliflower structure at 1000 °C (a)–(c), HRTEM micrographs showing the turbostratic carbon matrix with clear graphite crystallites (d)–(f), Raman (g) and XRD (h) of W1000.

and crystalline graphite. As shown a broad and weak diffraction peak was observed at about $43^{\circ}_{(100)}$ (turbostratic structure) indicating the presence of amorphous graphitic carbon and lower ordering. Besides, the increase in pores at high temperatures due to the higher orientation freedom of the graphite crystallites has led to a decrease in the severity of reflection and

Table 2 Calculated parameters of O_2/N_2 adsorption kinetic models at 6 bar for the W1000

		298 °K		308 °K		318 °K	
Kinetic models	Parameters	O_2	N_2	O_2	N_2	O_2	N_2
Pseudo-first-order	q_e (mmol g^{-1})	2.334	1.835	1.285	1.08	0.961	0.676
	k_f (min^{-1})	0.035	0.029	0.016	0.023	0.029	0.017
	R^2 (%)	0.9849	0.9598	0.9859	0.9668	0.9105	0.8766
Pseudo-second-order	q_e (mmol g^{-1})	2.384	1.896	1.340	1.118	0.965	0.721
	k_s (min^{-1})	0.0339	0.0274	0.0228	0.0398	0.1544	0.0314
	R^2 (%)	0.9961	0.9848	0.9977	0.9879	0.8865	0.9356
Elovich	(mmol g^{-1} min^{-1}) α	2.3×10^8	1.1×10^4	5.5×10^4	6.4×10^4	9.1×10^5	30.37
	β (g $mmol^{-1}$)	0.099	0.132	0.084	0.071	0.041	0.088
	R^2 (%)	0.9565	0.9858	0.8898	0.9191	0.8942	0.9126
Fractional-order	q_e (mmol g^{-1})	2.662	1.376	1.306	1.376	1.637	0.711
	k_n (min^{-1})	0.0685	0.055	0.0651	0.055	0.0036	0.0103
	n	3.0041	6.5344	0.949	6.5344	19.035	0.4638
	m	0.5458	1.2209	0.5273	1.2209	0.0001	0.1353
	R^2 (%)	0.9987	0.9933	0.9982	0.9933	0.8977	0.9782

expansion at peaks. The absence of a peak at $22^{\circ}_{(002)}$ (oriented aromatic carbon) is a sign of the structure's strong tendency to formation of highly disordered and randomly oriented graphitic carbon layers that generate higher specific surface areas, consistent with the observation of Raman and BJH's results. Raman results likewise revealed a more disordered structure, while XRD correlated to lower graphitization degrees.[51,80,91–93]

4.2 Adsorption kinetic and equilibrium isotherms

The gas adsorption processes by porous material is depending on micropores, mesoporous, surface area of adsorbent, and type of different kinetics. Review and analysis of the uptake kinetics reveal that the adsorbents' physical and chemical nature also affects the mechanism. We applied several theoretical kinetic models such as the pseudo-first-order, pseudo-second order, Elovich, and fractional-order kinetic models (eqn (6)–(9)) for kinetic models study.[94]

$$q_t = q_e(1 - e^{-k_1 t})\ \text{pseudo-first-order} \quad (6)$$

$$q_t = (q_e^2 k_s t)/[1 + q_e k_s t]\ \text{pseudo-second-order} \quad (7)$$

$$q_t = (1/\beta \ln(\alpha\beta)) + (1/\beta \times \ln t)\ \text{Elovich} \quad (8)$$

$$q_t = q_e - (q_e^{(1-n)} + ((n-1)/m)k_n t^m)^{(1/(1-n))}\ \text{fractional-order kinetic model} \quad (9)$$

The pseudo-first-order model shows the reversible adsorption with the equilibrium between the adsorbent surface and the pseudo-second-order kinetic model based on the chemisorption process as the adsorption controlling factor. The fractional-order kinetic model shows simultaneous physical and chemical adsorption. Due to the complexity of predicting kinetic parameters, a common approach involves adapting experimental data to a set of mentioned models and selecting one of the best options. The kinetic parameters are presented in Table 2 and the best model is based on correlation coefficient values (R^2) in the range of 0.8766 to 0.9987 at 298 °K, 308 °K, 318

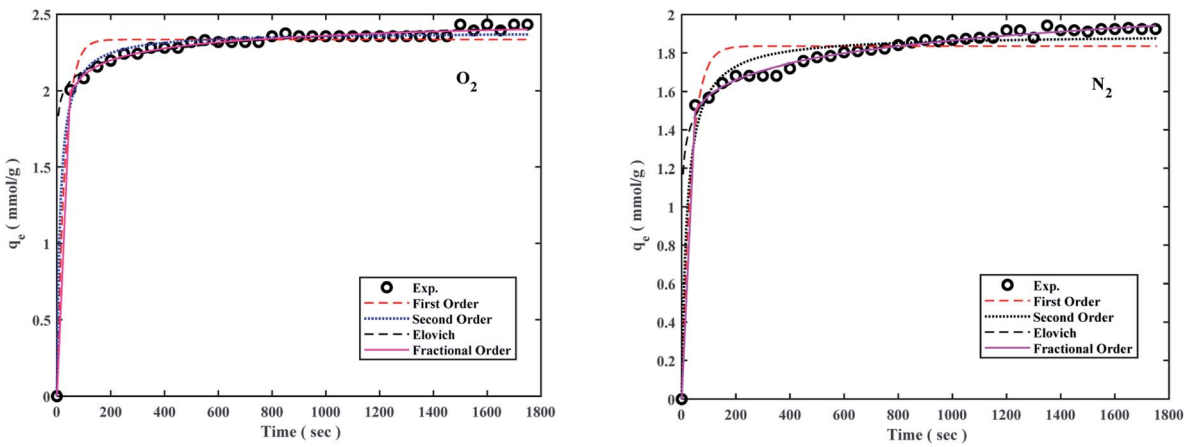

Fig. 7 O_2/N_2 adsorption capacities of the W1000 and corresponding fit desirable kinetic models at 298 °K and 6 bar.

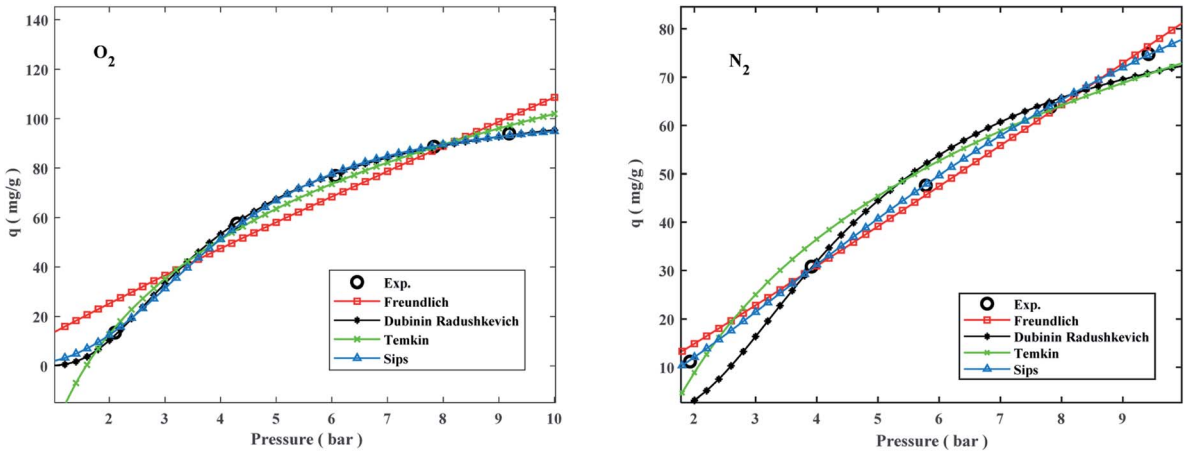

Fig. 8 Comparison of isotherms and O_2/N_2 experimental on the W1000 at 298 °K.

°K, and 6 bar were fitted. The results of the models were also plotted to the experiment data to describe the best kinetic model for O_2/N_2 adsorption, and the kinetic curves of the sorbent are shown in Fig. 7. Fig. 7 shows that the experimental data did not fit the first-order kinetic model, although fractional-order and second-order models were more proportionate.[26,95,96]

The kinetic parameters derived from Table 2 revealed that the fractional-order kinetic model was better appropriate for explaining adsorption kinetics. Furthermore, R^2 coefficient values for the fractional model ranged from 0.8977 to 0.9987, indicating that the fractional model was well fitted at 298 °K and 6 bar for O_2/N_2.

Adsorption isotherms by the following Freundlich, Dubinin–Radushkevich (D–R), Temkin, and sips models were plotted at 298 °K in the range of pressures 2 to 9 bar in Fig. 8. The experimental data and related correlation coefficient of R^2 for all coefficients of isotherm parameters models were obtained in Table 3. The decrease in K_f value revealed the physical adsorption behavior, while the increase in q_m value revealed the pressure and temperature-dependent O_2/N_2 adsorption behavior.[94]

The q_e values decreased as the temperature was increased, indicating an exothermic O_2/N_2 adsorption behavior. All of the isotherm models good agreed with the experimental data but the Sips isotherm model has gained the highest correlation coefficient (R^2) values fitted with experimental data. The Sips model proposed a similar equation to the Freundlich model for distinguishing the problem of the ongoing increase in the value adsorbed at increasing in limited pressure for the Freundlich model.[97] Furthermore, the beneficial data assigned to the energy parameters is provided by two isotherm models

Table 3 Isotherm models of O_2/N_2 adsorption for the sorbent at 6 bar[a]

		298 °K		308 °K		318 °K	
Models	Parameters	O_2	N_2	O_2	N_2	O_2	N_2
Freundlich $q_e = k_F P_e^{1/n}$	k_F	13.547	7.145	7.764	6.322	6.112	2.808
	n	1.106	0.946	0.983	1.007	0.951	0.860
	R^2	0.9633	0.9968	0.9898	0.9929	0.9955	0.9998
Dubinin–Radushkevich $q_e = q_m e^{-\lambda\omega^2}$	q_m	108.607	86.996	85.399	68.661	73.536	46.474
	λ	2.409	3.398	3.253	3.420	3.304	4.337
	ω	0.456	0.384	0.392	0.382	0.389	0.340
	R^2	0.9997	0.9867	0.9910	0.9910	0.9851	0.9835
Temkin $q_e = B \times \log(A) + B \times \log(c)$	A	0.630	0.624	0.599	0.628	0.597	0.604
	B	55.402	39.913	41.138	31.265	35.101	19.837
	R^2	0.9967	0.9870	0.9953	0.9923	0.9901	0.9694
Sips $q_e = \frac{q_m (bP)^{1/n}}{1 + (bP)^{1/n}}$	q_m	1.966	4.345	2.928	2.845	3.481	2.543
	bP	2.858	1.601	1.985	1.820	1.651	1.272
	n	0.0193	0.0307	0.0285	0.0328	0.0302	0.0094
	R^2	0.9995	0.9999	1.0000	1.0000	0.9995	1.0000

[a] Where q_e is the value of O_2/N_2 adsorption capacity (mmol g^{-1}), q_m is the max adsorption value of O_2/N_2 (mmol g^{-1}), P is the equilibrium pressure (bar), K_F is the Freundlich model constants [(mmol g^{-1}). (bar^{-1})$^{1/n}$)] and n is Freundlich isotherm constant. λ is (D–R) model constant (mol^2 J^{-2}), ω is Polanyi potential (J mol^{-1}), A is the Temkin model constant (L mol^{-1}), and B is the first virial coefficient ($B = RT \times b_T^{-1}$);b_T^{-1} (J mol^{-1}).

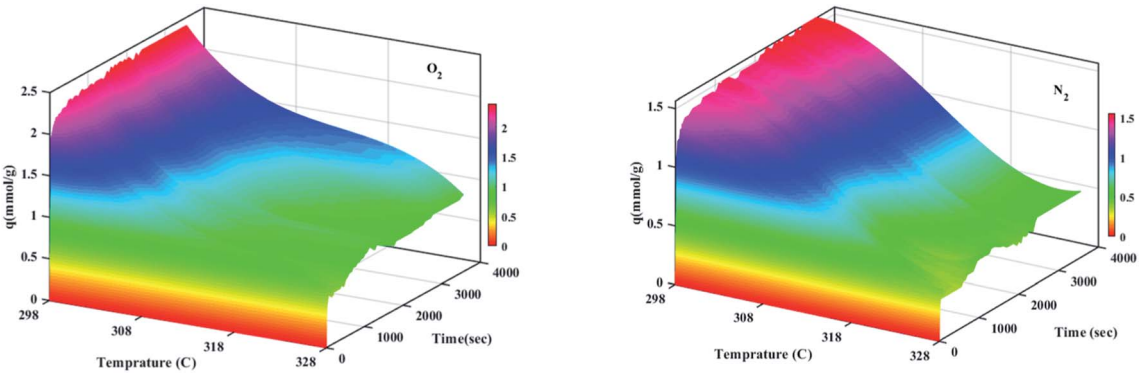

Fig. 9 Temperature effect on the O_2/N_2 adsorption capacity of the W1000 at 6 bar for 60 min.

developed by D–R and Temkin, where ω is the mean adsorption free energy and b_T is the heat of adsorption. The normal physisorption of O_2/N_2 adsorption is shown by average λ values in the 3–4 (kJ mol^{-1}) range. The Freundlich constant, n, in the range of 1 to 2, illustrates the desirability of physisorption based on the findings of Table 3. The adsorption process is multilayer, according to the findings, with O_2/N_2 adsorbed and penetrated in the surface and inner layers of the sorbent. According to the Sips model, more efficient contact sites are prioritized, meaning that the sorbent surface is heterogeneous and multilayer O_2/N_2 adsorption is induced by a nonhomogeneous distribution of energy inactive sites.[94,98,99] This point in the Sips model represents the physical adsorption process. Furthermore, the isotherm parameters derived from Table 3 revealed that the Sips isotherm model was better appropriate for explaining adsorption isotherm. The coefficient values of the Sips model ranged from 0.9995 to 1, indicating that the Sips model was well fitted from range 298 °K to 308 °K and 6 bar for O_2/N_2 adsorption. According to the correlation coefficient (R^2) values derived in Table 3, the strength of the indicated isotherms models in the description and prediction of adsorption behavior was Sips > Freundlich > D–R > Temkin.[94]

4.3 The effect of temperature and pressure on O_2/N_2 adsorption

The effect of different temperatures at 6 bar for 60 min on the W1000 for review of O_2/N_2 adsorption capacity by adsorption setup is shown in Fig. 9. As can be seen, the increase of temperature from 298 °K to 398 °K, reduced the O_2/N_2 adsorption capacity for the W1000, and the maximum adsorption capacity of both gases was observed at 298 °K. The first thing to cite about the results in Fig. 9 is that denotes the relatively low quantity of N_2 adsorbed, resulting in the very interesting selectivity values recorded for W1000. The second thing to cite these results is that the O_2 is more quickly than N_2 adsorbed at the same time, resulting again in selectivity values recorded for W1000.[100] Furthermore, the results show that the O_2/N_2 adsorption process is exothermic, and O_2/N_2 adsorption capacity decreases by increasing the temperature. The effect of equilibrium pressure in the range of 298 °K to 398 °K on the W1000, W1000-B, W1000-Ar, and W1000-Ar-B sample sorbents for adsorption capacities of O_2/N_2 is plotted in Fig. 10. The results show that the W1000 sample is higher efficiency in the adsorption capacity of O_2 and N_2. Increased pressure has

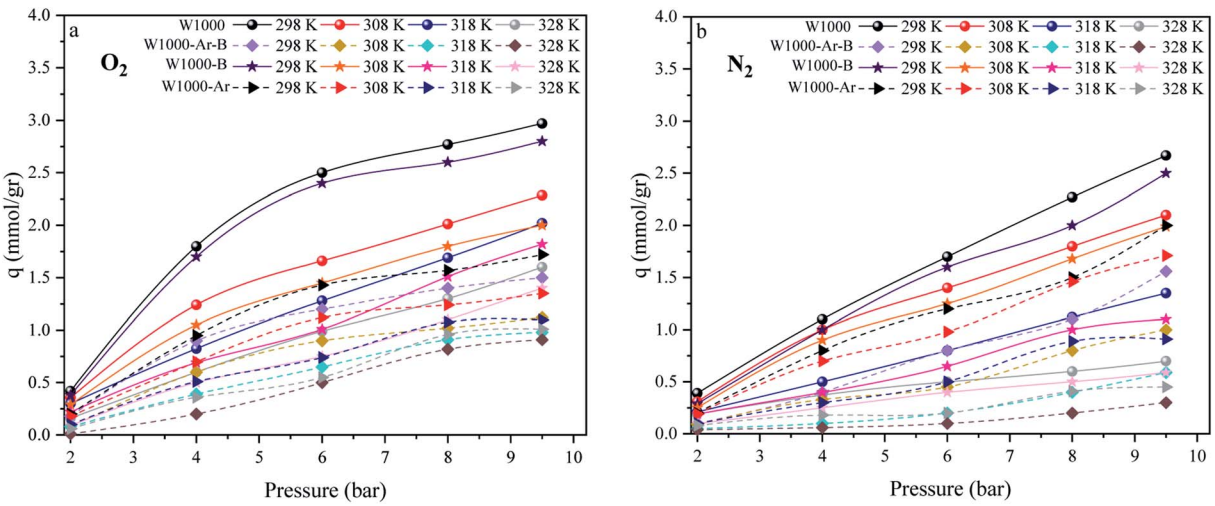

Fig. 10 The O_2/N_2 adsorption equilibrium isotherms (a) O_2, (b) N_2 of the W1000, W1000-B, W1000-Ar-B, and W1000-Ar.

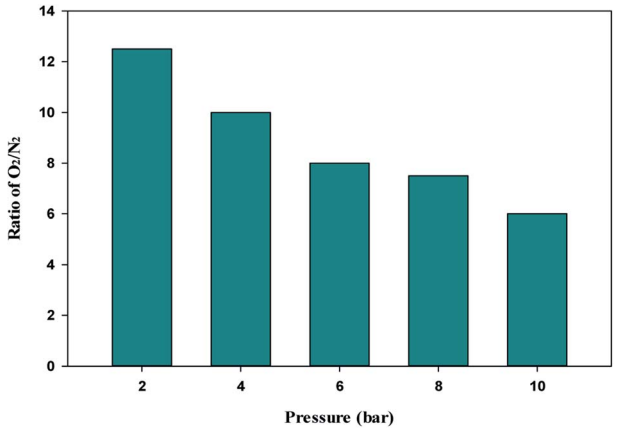

Fig. 11 O_2/N_2 adsorption selectivity on W1000 at 298 K and different pressures.

a significant impact on O_2/N_2 adsorption capability, according to the findings. At 9.2 bar and 298 °K, the maximum adsorption capacities of O_2/N_2 on the sorbent are 2.94 (mmol g^{-1}) and 2.67 (mmol g^{-1}), respectively.

The single-component isotherm is a technique for determining the selectivity of adsorbent for O_2 over N_2. The equation was used to calculate the adsorption selectivity of O_2 over N_2.[101]

$$\alpha = (V_{O_2}/V_{N_2}) \quad (10)$$

V_{O_2} and V_{N_2} are the volumes of O_2 and N_2 gas adsorbed at a given pressure P and temperature T, respectively. The W1000 separation performance was evaluated using the reported equation. At various pressures, the selectivity of O_2 over N_2 was determined, and the results are presented in Fig. 11. As can be observed from the results, the W1000 performed better in O_2 adsorption than N_2, implying that it has more potential for selective adsorption.

4.4 Comparison of O_2/N_2 uptake

The high adsorption values of these two gases indicate the principal role of mesopores and oxyfunctionalized groups in the sorption and compensation of nitrogen deficiency in the structure. In a selective adsorption application, the pore size and shape are the most significant characteristics. The void areas between highly irregular graphitic plates provide porous carbons pore structure. Moreover, the electrical characteristics of the adsorbate, such as the dipole/quadrupole moment and/or polarizability, influence the rate of sorption. Otherwise, the kinetic diameter, molecular size, and the structure of N_2/O_2, affect the rate of adsorption. As shown in Fig. 10, at a specified temperature and pressure, porous carbon tends to adsorb more oxygen than nitrogen. Charge transfer from micro graphite to adsorbed oxygen occurs as adsorbed oxygen molecules penetrate smaller pores (microporosities). Owing to the abundance of micropores, this indicates a greater tendency of these pores to adsorb more oxygen. The kinetic diameter of a molecule in a gas is proportional to its mean free path, which indicates the size of the molecule as a target. As a result, the kinetic diameter differs from the atomic diameter, measured in terms of the atom's electron shell size, which is generally significantly smaller. The kinetic diameters of O_2 and N_2 are 3.46 and 3.64 Å, respectively. These values are so near that separating them using a size exclusion or molecular sieve technique is difficult.[94,102,103] O_2 has a somewhat lower effective kinetic diameter within porous materials than N_2 from a kinetic viewpoint. As a result, O_2 diffusion *via* sorbent meso–micro pores can be

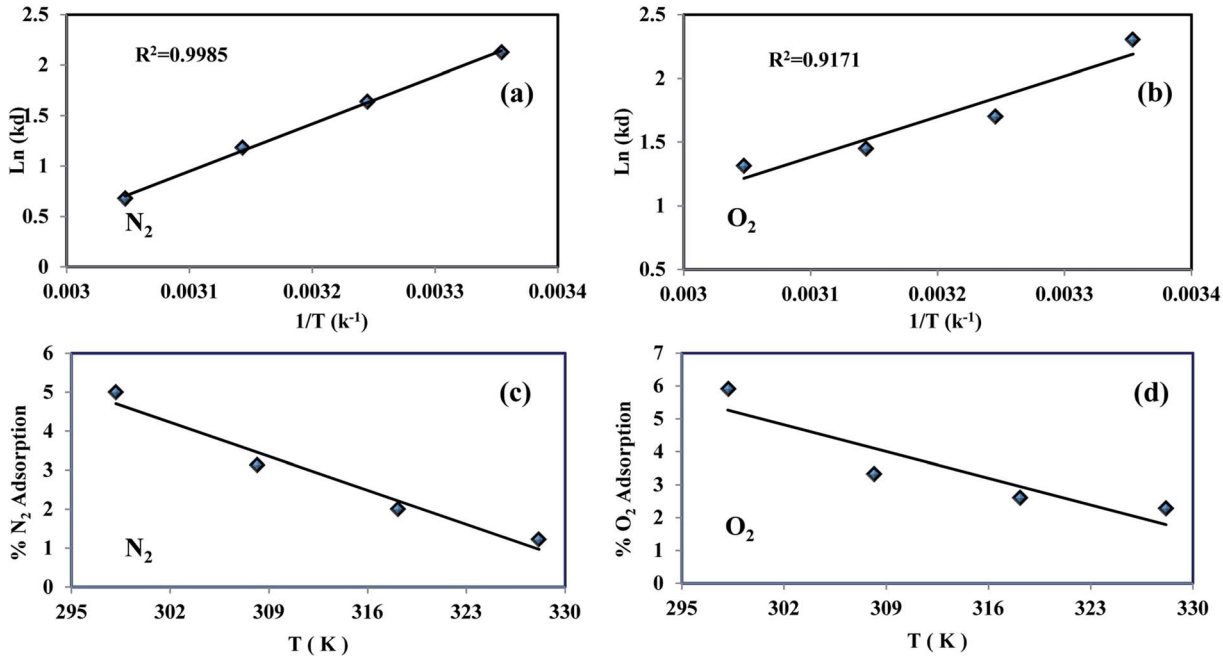

Fig. 12 O_2/N_2 experimental Van't Hoff plot (a and b) and adsorption variations percentage *vs.* temperature (c and d).

Table 4 Thermodynamic parameters of the W1000 in O_2/N_2 adsorption at 6 bar

Gas	ΔH (kJ mol^{-1})	ΔS (kJ mol K)	ΔG (kJ mol^{-1}) 298 °K	308 °K	318 °K	328 °K
O_2	−26.449	−0.071	−5.428	−4.723	−4.018	−3.312
N_2	−39.079	−0.113	−5.310	−4.178	−3.045	−1.912

quicker than N_2 diffusion, particularly when the adsorbent contains reasonably uniform pores with diameters near the kinetic diameter of N_2.[104] Furthermore, nitrogen and oxygen have a shape factor that is likely to affect (adverse) adsorption kinetics since these molecules must pass through the selective porosity longitudinally, resulting in a loss of rotational flexibility.[105] Because activation of porous carbon and high temperatures enlarge pore diameters, it is predicted that N_2 contact with pore walls will be reduced more than O_2 interaction.[106] The quadrupole moment of N_2 (-4.9×10^{-26} cm^2) is approximately four times that of O_2, resulting in increased N_2 adsorption, as is well known. Thus, N_2 can have a stronger interaction with the sorbent's electrical field gradients than O_2. However, by observing the obtained results, it can be understood that this factor does not play a role in the adsorption rate of gases on porous carbon.[100] Because of the diamagnetic nature of nitrogen molecules, the dipolar field of paramagnetic oxygen molecules shows better adsorption at very high pressures. The reason for this is that the electron spin resonance does not change for nitrogen molecules at very high pressures.[107]

4.5 Adsorption thermodynamic analysis

The standard free energy (ΔG^0), enthalpy (ΔH^0), and entropy (ΔS^0) are thermodynamic parameters and calculated using the following equations:

$$\Delta G^0 = \Delta H^0 - T\Delta S^0 \quad (11)$$

$$\Delta G^0 = -RT \ln K_d \quad (12)$$

$$\ln K_d = \frac{\Delta S^0}{R} - \frac{\Delta H^0}{RT} \quad (13)$$

$$K_d = (P_i - P_e) \times (V/W) \quad (14)$$

The values of (ΔH^0) and (ΔS^0) were calculated from the slope and cut off the plot of Ln K_d *versus* $1 \times T^{-1}$. The standard Gibbs free energy change of sorption (ΔG^0) was calculated using equations eqn (11) and (12). The Van't Hoff equation was used through equations eqn (11) and (14). In the mentioned equations, R is gas constant (8.314 (J mol^{-1} K^{-1})).[14] As can be seen in

Table 5 Experimental parameter ranges of various biomass *vs.* the present study.[110]

Precursors (−)	Pyrolysis temperature (°C)	Specific surface area (m^2 g^{-1})	Porosity volume (cm^3 g^{-1})
Lignin waste	600–700	1820–2038	0.91–1
Crab shell	500–650	192–1387	0.09–0.5
Peanut shell	680–780	1713–1871	0.73–0.8
Empty fruit bunch	600–800	1080–1120	0.17–0.43
Olive stone	800	1063	0.49
Bambo	873–973	1840–1990	0.7–0.8
Pollen	800	937	0.4
Popcorn	800	867–1489	0.40–0.70
Lotus leaf	450–500	792–1924	0.29–0.79
Vine shoots	700–800	538–1439	0.23–0.67
Chitosan	800–1000	1389–2025	0.68–1.15
Poplar wood	600	511	0.22
Waste wool	600	1010–1420	0.57–0.86
Chrysanthemum tea	1000	1840	1.16
Cork	700	2010	0.82
Coffee ground	700–800	1476–1692	0.61–0.71
Garlic peel	600–800	967–1262	0.51–0.7
Wheat	700	1438	0.65
Pineapple	700	1076	0.08
Coconut shell	600	1172	0.43
Paulownia sawdust	600–900	782	0.41–1.181
Walnut-shell	500	811	0.34
Peanut shell-C	973	956	0.43
Sunflower seed shell	973	1790	0.77
Catkin	700–900	1005–1455	0.4–0.78
Tar	800	1829	1.2
Sugarcane bagasse	750	622	0.38
Tea seed shell	700	1064	0.47
This work (walnut-shell)	**1000**	**2042.4**	**2.68**

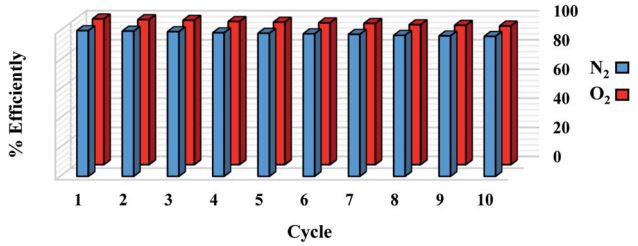

Fig. 13 Recycling performance of the W1000 for O_2/N_2 adsorption.

Fig. 12(a) and (b) the values (ΔH^0) and (ΔS^0) were calculated from the slope and traverse of the plot of Ln K_d unto $1 \times T^{-1}$. The results of calculated thermodynamic parameters of O_2/N_2 were tabulated in Table 4. The value of $\Delta H^0 < 20$ (kJ mol^{-1}) represented the physisorption process and if the value of $\Delta H^0 >$ 40 (kJ mol^{-1}), represents the chemisorption. The ΔS^0 is represented the randomized and organized interfaces of gas and solid, which in the case of $\Delta S^0 > 0$, it was more random, and in the case of $\Delta S^0 < 0$ it was less random.[108,109] The Van't Hoff plot of the equilibrium constant of the sorbent which was used for the estimate of ΔS^0 and ΔH^0 in the range of temperature from 298 °K to 328 °K was plotted in Fig. 12(a and b). The negative values of Gibbs free energy change (ΔG^0) and (ΔS^0), indicating that the adsorption process is exothermic and spontaneous.

The percentage variations of O_2/N_2 adsorption into temperature were shown in Fig. 12(c and d). The percentage of adsorption capacity for both gases increases with decreasing temperature, which confirms this physisorption process.

4.6 Comparison of various porous carbon

The recent experimental data on biomass-derived precursors for porous carbon adsorbents are summarized in Table 5. The current derived porous carbon fine sample has a considerably greater porosity volume capacity than previous experimental studies due to its high surface area and hierarchical porosity. The high surface area (2042.4 m^2 g^{-1}), accessible micro–meso pores, and a reasonable percentage of micropores in W1000 contribute to its excellent capacitance, as seen in Table 1.

Table 6 compares the adsorption capacities of the porous carbon used in this study to a variety of other adsorbents previously used for O_2/N_2 adsorption. As shown, the W1000 has much higher adsorption capacities than many other previously reported adsorbents. The findings of this research can be used to develop a new porous carbon green synthesis adsorbent that is both effective and high performance for O_2/N_2 adsorption.

4.7 Regeneration performance of W1000 studies

The reuse of sorbent for economic reasons is one of the most significant considerations. For 1 g sorbent, the regeneration

Table 6 Comparison of the O_2/N_2 adsorption capacities of the porous carbon derived from walnut-shell with other works

Material (manufacture)	Test method	Surface area (m^2 g^{-1})	O_2/N_2 adsorption (mmol g^{-1})	Pressure (bar)	Temperature (K)	Ref.
5A/3A MSC (Takeda)	VSM	—	0–1.76/0–1.75	0–8	273–323	111
ACF (Kurare)	ESR	2000	0.181/0.064	0–0.02	298	107
CMS 3A (Takeda)	Volumetric	—	0.63/0.62	0–2.2	293	112
			0.35/0.36		323	
			0.21/0.23		353	
CMS-T3A (Takeda)	Volumetric	522.59	2.2/1.2	0–5	293	113
			1.8/0.85		303	
			1.7/0.75		313	
AC (AX-21); (coconut shells based using KOH impregnated)	Volumetric	3000	9/—	2.5	118	98
			2.5/—	10	298	
			2.1/—	10	313	
CMS 3A (Takeda)	Gravimetric	523	0.07/0.22	0.69/0.68	293	97
			0.07/0.16	0.69/0.64	303	
			0.06/0.13	0.72/0.65	313	
CMB (palm shell based using PEI impregnated)	Micrometrics	1052	0.4/0.29	0–1	298	35
AC (SorboNorit B3)	Volumetric	1012	1.75/—	9.96	303	114
			2.63/—	19.02		
			3.39/—	31.5		
AC	Volumetric	1306.4	1.519/—	10.1	323	94
CMS		436.8	1.18/1.06	9.56	323	
AC			1.86/1.24	10.26	308	
CMS			1.39/—	9.78	308	
AC			2.23/—	10.17	293	
CMS (Kuraray)			1.66/1.45	10.1	293	
CMS GC-AP (air products and chemicals)	Volumetric	—	0.88/0.78	7	298	99
Porous carbon (walnut-shell based using self-activation method)	**Volumetric**	**2042.4**	**2.4/1.7**	**6**	**298**	**This work**
	Volumetric	**2042.4**	**2.94/2.67**	**9.2**	**298**	**This work**

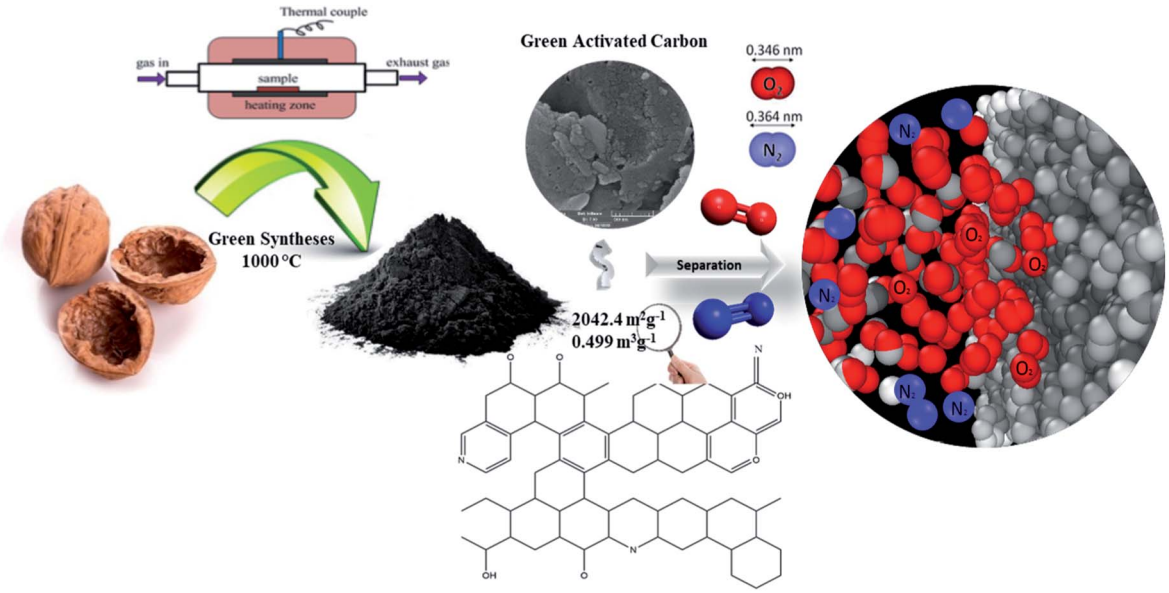

Fig. 14 Schematic representation of the porous carbon synthesis for O_2/N_2 adsorption.

process was measured at a pressure of less than 2 bar. For the O_2/N_2 adsorption operation, 10 adsorption/desorption cycles were reported at 298 °K at 6 bar and regenerated at 450 °K in a vacuum oven for 6 hours. As seen in Fig. 13, there is no significant change in adsorbent potential after each loop. After 10 cycles, the adsorption performance of the sorbent was reduced from 100% to 96%. According to the effects of the regeneration process, the sorbent can be used in industrial applications as a low-cost and cost-effective adsorbent. The steps involved in the processing and synthesizing the sorbent are depicted in Fig. 14.

5 Conclusions

In this research, a high-performance adsorbent for O_2/N_2 adsorption is developed using a new green synthesis of porous carbon adsorbent based on the green self-activation process. In summary, a mesopore-dominant porous carbon was synthesized with a high surface area *via* direct carbonization of walnut-shell. The optimal porous carbon possesses the specific surface area and the pore volume up to 2042 ($m^2\ g^{-1}$) and 2.68 ($cm^3\ g^{-1}$) at 1000 °C, respectively. During the characterization of the optimal sample, the open porosity with the formation of hierarchically interconnected porous, and turbostratic structures was identified. The mechanism of the self-activating system confirms the effective role of gases emitted from the carbon precursor (such as CO and CO_2) in the activation of porous carbon. The green porous carbon preparation confirms an important perspective on the separation efficiency of O_2 and N_2 gases. Adsorption experiments in the temperature range of 298 °K to 328 °K under pressures up to 9.5 bar were conducted. The kinetics of O_2/N_2 adsorption on the sorbent has followed the fractional-order kinetic model well and thermodynamic analysis indicated that physisorption process is govern. The sips, fractional-order, and pseudo-second-order isotherm models were well equipped with adsorption isotherm and kinetic adsorption models, respectively, after comparing experimental adsorption effects by models. It was found that the factors such as the kinetic diameter of gases, the dipole/quadrupole moment, polarizability, and the abundance of micropores play a crucial role in better oxygen uptake than nitrogen. The maximal adsorption potential for O_2/N_2 was found to be 2.94 (mmol g^{-1}) and 2.67 (mmol g^{-1}) at 298 °K under 9.5 bar pressure, respectively. After ten cycles, the adsorption efficiency of the sorbent was reduced from 100% to 96%. Compared to the other carbon-based adsorbents studied, due to the high-performance efficiency and high-efficiency regeneration, the prepared sorbent can be promising for industrial air separation technologies based on the advanced adsorbents. In semi-scale and industrial processes, the new approach reflects a promising technique for preparing the green porous carbon from biomass wastes.

Nomenclature

A	Temkin model constant (L mol^{-1})
B	First virial coefficient
C	Second virial coefficient
f	Subscripts refer to final condition
i	Subscripts refer to initial condition
k_L	Langmuir model constant (bar^{-1})
k_f	Rate constant of adsorption for the pseudo-first-order (min^{-1})
k_F	Freundlich model constants [(mmol g^{-1}) (bar^{-1})$^{1/n}$)]
k_s	Rate constant of adsorption for the first-order model (g $mmol^{-1}$ min^{-1})
k_n	Rate constant of adsorption for the fractional-order model (min^{-1})
K_d	Distribution coefficient
m	Mass of gas adsorbed (mg)

M_w Molecular weight of gas (g mol^{-1})
P Pressure (bar)
P_0 Saturated vapor pressure (bar)
P_e Equilibrium pressure (bar)
q Adsorption capacity (mmol g^{-1}), (mg g^{-1})
q_e Equilibrium adsorption capacity (mmol g^{-1})
q_m Maximum adsorption (mmol g^{-1})
q_t Adsorption capacity at specified time t (mmol g^{-1})
R Universal gas constant (8.314 J mol^{-1} K^{-1})
R^2 Correlation coefficient (%)
T Temperature (°K), (°C)
t Time (s)
w Mass of adsorbent (g)
Z Compressibility factor

Greek symbols

α Parameter value of Elovich model (mmol g^{-1} min)
β Parameter value of Elovich model (g mmol^{-1})
λ Dubinin–Radushkevich (D–R) model constant (mol^2 J^{-2})
ω Polanyi potential (J mol^{-1})

Acronyms

AC	Activated carbon
ACF	Activated carbon fiber
CMS	Carbon molecular sieve
CMB	Carbon molecular basket
DTA	Differential thermal analysis
ESR	Electron spin resonance
FESEM	Field emission scanning electron microscopy
FTIR	Fourier transform infra-red
HRTEM	High-resolution transmission electron microscopy
MSC	Molecular sieve carbon
MOFs	Metal–organic frameworks
PEI	Poly ethylene imine
PSA	Pressure swing adsorption
PSD	Pore size distribution
TGA	Thermo gravimetric analysis
VSM	Vacancy solution model
XPS	X-ray photoelectron spectroscopy
XRD	X-ray diffraction

Conflicts of interest

The authors declare that they have no known competing financial interests or personal relationships that could have appeared to influence the work reported in this paper.

References

1 D. Ferreira, P. Barcia, R. D. Whitley and A. l. Mendes, *Ind. Eng. Chem. Res.*, 2015, **54**, 9591–9604.
2 A. Marcinek, J. Guderian and D. Bathen, *Adsorption*, 2021, 1–16.
3 S. P. Reynolds, A. D. Ebner and J. A. Ritter, *Ind. Eng. Chem. Res.*, 2006, **45**, 3256–3264.
4 J. Santos, P. Cruz, T. Regala, F. Magalhaes and A. Mendes, *Ind. Eng. Chem. Res.*, 2007, **46**, 591–599.
5 M. L. Zanota, N. Heymans, F. Gilles, B. L. Su, M. Frère and G. De Weireld, *J. Chem. Eng. Data*, 2010, **55**, 448–458.
6 T. Burdyny and H. Struchtrup, *Energy*, 2010, **35**, 1884–1897.
7 N. Zhang and N. Lior, *Energy*, 2008, **33**, 340–351.
8 G. Bello, R. García, R. Arriagada, A. Sepulveda-Escribano and F. Rodrıguez-Reinoso, *Microporous Mesoporous Mater.*, 2002, **56**, 139–145.
9 F. E. Epiepang, X. Yang, J. Li, Y. Liu and R. T. Yang, *AIChE J.*, 2018, **64**, 406–415.
10 M. J. Kirschner, A. Alekseev, S. Dowy, M. Grahl, L. Jansson, P. Keil, G. Lauermann, M. Meilinger, W. Schmehl and H. Weckler, *Ullmann's encyclopedia of industrial chemistry*, 2000, pp. 1–32.
11 X. Li, L. Zhang, Z. Yang, P. Wang, Y. Yan and J. Ran, *Sep. Purif. Technol.*, 2020, **235**, 116213.
12 D. M. Ruthven, *Principles of adsorption and adsorption processes*, John Wiley & Sons, 1984.
13 P. Li and F. H. Tezel, *Microporous Mesoporous Mater.*, 2007, **98**, 94–101.
14 Y. Fu, Y. Liu, X. Yang, Z. Li, L. Jiang, C. Zhang, H. Wang and R. T. Yang, *Appl. Surf. Sci.*, 2019, **480**, 868–875.
15 X. Yang, F. E. Epiepang, J. Li, Y. Wei, Y. Liu and R. T. Yang, *Chem. Eng. J.*, 2019, **362**, 482–486.
16 A. Jayaraman, R. T. Yang, S.-H. Cho, T. S. Bhat and V. N. Choudary, *Adsorption*, 2002, **8**, 271–278.
17 G. Férey, *Chem. Soc. Rev.*, 2008, **37**, 191–214.
18 D. A. Reed, D. J. Xiao, M. I. Gonzalez, L. E. Darago, Z. R. Herm, F. Grandjean and J. R. Long, *J. Am. Chem. Soc.*, 2016, **138**, 5594–5602.
19 L. Melag, M. M. Sadiq, S. J. Smith, K. Konstas, K. Suzuki and M. R. Hill, *J. Mater. Chem. A*, 2019, **7**, 3790–3796.
20 K. Sumida, D. L. Rogow, J. A. Mason, T. M. McDonald, E. D. Bloch, Z. R. Herm, T.-H. Bae and J. R. Long, *Chem. Rev.*, 2012, **112**, 724–781.
21 H. Demir, S. J. Stoneburner, W. Jeong, D. Ray, X. Zhang, O. K. Farha, C. J. Cramer, J. I. Siepmann and L. Gagliardi, *J. Phys. Chem. C*, 2019, **123**, 12935–12946.
22 Q. M. Wang, D. Shen, M. Bülow, M. L. Lau, S. Deng, F. R. Fitch, N. O. Lemcoff and J. Semanscin, *Microporous Mesoporous Mater.*, 2002, **55**, 217–230.
23 J. B. DeCoste, M. H. Weston, P. E. Fuller, T. M. Tovar, G. W. Peterson, M. D. LeVan and O. K. Farha, *Angew. Chem.*, 2014, **126**, 14316–14319.
24 D. A. Reed, D. J. Xiao, H. Z. Jiang, K. Chakarawet, J. Oktawiec and J. R. Long, *Chem. Sci.*, 2020, **11**, 1698–1702.
25 G. Arora and S. I. Sandler, *J. Chem. Phys.*, 2006, **124**, 084702.
26 A. T. Nasrabadi and M. Foroutan, *Comput. Mater. Sci.*, 2012, **61**, 134–139.
27 F. Vallejos-Burgos, F.-X. Coudert and K. Kaneko, *Nat. Commun.*, 2018, **9**, 1–9.

28 E. D. Bloch, W. L. Queen, M. R. Hudson, J. A. Mason, D. J. Xiao, L. J. Murray, R. Flacau, C. M. Brown and J. R. Long, *Angew. Chem.*, 2016, **128**, 8747–8751.
29 P. Giannozzi, R. Car and G. Scoles, *J. Chem. Phys.*, 2003, **118**, 1003–1006.
30 S. Chen, Z. Wang, Y. Xia, B. Zhang, H. Chen, G. Chen and S. Tang, *RSC Adv.*, 2019, **9**, 25480–25487.
31 L. Zhu, D. Shen and K. H. Luo, *J. Hazard. Mater.*, 2020, **389**, 122102.
32 J. E. Sosa, C. Malheiro, R. P. Ribeiro, P. J. Castro, M. M. Piñeiro, J. M. Araújo, F. Plantier, J. P. Mota and A. B. Pereiro, *J. Chem. Technol. Biotechnol.*, 2020, **95**, 1892–1905.
33 P. González-García, *Renewable Sustainable Energy Rev.*, 2018, **82**, 1393–1414.
34 J. Feng, R. Tang, X. Wang and T. Meng, *ACS Appl. Energy Mater.*, 2021, **4**, 5230–5236.
35 M. K. Aroua, W. M. A. W. Daud, C. Y. Yin and D. Adinata, *Sep. Purif. Technol.*, 2008, **62**, 609–613.
36 H. Sun, B. Yang and A. Li, *Chem. Eng. J.*, 2019, **372**, 65–73.
37 H. B. M. Emrooz, M. Maleki, A. Rashidi and M. Shokouhimehr, *Biomass Convers. Biorefin.*, 2020, 1–12.
38 J. Maciá-Agulló, B. Moore, D. Cazorla-Amorós and A. Linares-Solano, *Microporous Mesoporous Mater.*, 2007, **101**, 397–405.
39 M. Xu, D. Li, Y. Yan, T. Guo, H. Pang and H. Xue, *RSC Adv.*, 2017, **7**, 43780–43788.
40 R. Acosta, V. Fierro, A. M. De Yuso, D. Nabarlatz and A. Celzard, *Chemosphere*, 2016, **149**, 168–176.
41 J. Lee, J. Kim and T. Hyeon, *Adv. Mater.*, 2006, **18**, 2073–2094.
42 E. Pérez-Mayoral, I. Matos, M. Bernardo and I. M. Fonseca, *Catalysts*, 2019, **9**, 133.
43 J. He, D. Zhang, M. Han, X. Liu, Y. Wang, Y. Li, X. Zhang, K. Wang, H. Feng and Y. Wang, *Journal of Energy Storage*, 2019, **21**, 94–104.
44 F. Rodriguez-Reinoso and M. Molina-Sabio, *Carbon*, 1992, **30**, 1111–1118.
45 R. I. Kosheleva, A. C. Mitropoulos and G. Z. Kyzas, *Environ. Chem. Lett.*, 2019, **17**, 429–438.
46 H. Wang, C. Sheng, T. Cai, C. Jin, Q. Sun and C. Wang, *RSC Adv.*, 2018, **8**, 12204–12210.
47 J. Dai, S. Tian, Y. Jiang, Z. Chang, A. Xie, R. Zhang and Y. Yan, *J. Alloys Compd.*, 2018, **732**, 222–232.
48 J. Yin, W. Zhang, N. A. Alhebshi, N. Salah and H. N. Alshareef, *Small Methods*, 2020, **4**, 1900853.
49 G. Asimakopoulos, M. Baikousi, C. Salmas, A. B. Bourlinos, R. Zboril and M. A. Karakassides, *J. Hazard. Mater.*, 2021, **405**, 124274.
50 J.-W. Kim, M.-H. Sohn, D.-S. Kim, S.-M. Sohn and Y.-S. Kwon, *J. Hazard. Mater.*, 2001, **85**, 301–315.
51 X.-L. Zhu, P.-Y. Wang, C. Peng, J. Yang and X.-B. Yan, *Chin. Chem. Lett.*, 2014, **25**, 929–932.
52 G. Gou, F. Huang, M. Jiang, J. Li and Z. Zhou, *Renewable Energy*, 2020, **149**, 208–216.
53 S. Yu, N. Sun, L. Hu, L. Wang, Q. Zhu, Y. Guan and B. Xu, *J. Power Sources*, 2018, **405**, 132–141.
54 G. Wang, D. Wang, S. Kuang, W. Xing and S. Zhuo, *Renewable energy*, 2014, **63**, 708–714.
55 S. Sun, Q. Yu, M. Li, H. Zhao and C. Wu, *Renewable energy*, 2019, **142**, 11–19.
56 S. Wang and G. M. Lu, *Carbon*, 1998, **36**, 283–292.
57 J. Ou, Y. Zhang, L. Chen, Q. Zhao, Y. Meng, Y. Guo and D. Xiao, *J. Mater. Chem. A*, 2015, **3**, 6534–6541.
58 J. Niu, R. Shao, M. Liu, J. Liang, Z. Zhang, M. Dou, Y. Huang and F. Wang, *Energy Storage Materials*, 2018, **12**, 145–152.
59 G. Singh, K. S. Lakhi, S. Sil, S. V. Bhosale, I. Kim, K. Albahily and A. Vinu, *Carbon*, 2019, **148**, 164–186.
60 C. Bommier, R. Xu, W. Wang, X. Wang, D. Wen, J. Lu and X. Ji, *Nano Energy*, 2015, **13**, 709–717.
61 J. Hunt, A. Ferrari, A. Lita, M. Crosswhite, B. Ashley and A. Stiegman, *J. Phys. Chem. C*, 2013, **117**, 26871–26880.
62 C. Jiang, G. A. Yakaboylu, T. Yumak, J. W. Zondlo, E. M. Sabolsky and J. Wang, *Renewable Energy*, 2020, **155**, 38–52.
63 K. Sun, C.-y. Leng, J.-c. Jiang, Q. Bu, G.-f. Lin, X.-c. Lu and G.-z. Zhu, *N. Carbon Mater.*, 2017, **32**, 451–459.
64 J. Du, L. Liu, Z. Hu, Y. Yu, Y. Qin and A. Chen, *Adv. Funct. Mater.*, 2018, **28**, 1802332.
65 L. Yin, M. Park, I. Jeon, J. H. Hwang, J. P. Kim, H. W. Lee, M. Park, S. Y. Jeong and C.-R. Cho, *Electrochim. Acta*, 2021, **368**, 137630.
66 B. Kim, J. Park, S. Baik and J. W. Lee, *J. Porous Mater.*, 2020, **27**, 451–463.
67 X. Hu, X. Sun, Q. Song, Y. Zhu, Y. Long and Z. Dong, *Green Chem.*, 2020, **22**, 742–752.
68 E. M. Mistar, T. Alfatah and M. D. Supardan, *J. Mater. Res. Technol.*, 2020, **9**, 6278–6286.
69 X. Ma, C. Su, B. Liu, Q. Wu, K. Zhou, Z. Zeng and L. Li, *Sep. Purif. Technol.*, 2021, **259**, 118065.
70 M. S. Ansari, T. N. J. I. Edison and Y. R. Lee, *Sustainable Energy Fuels*, 2020, **4**, 5697–5708.
71 P. J. Wibawa, M. Nur, M. Asy'ari and H. Nur, *Heliyon*, 2020, **6**, e03546.
72 M. Doğan, P. Sabaz, Z. Biçil, B. K. Kizilduman and Y. Turhan, *J. Energy Inst.*, 2020, **93**, 2176–2185.
73 H. Xu, Y. Liu, H. Liang, C. Gao, J. Qin, L. You, R. Wang, J. Li and S. Yang, *Sci. Total Environ.*, 2021, **759**, 143457.
74 J. Yu, X. Li, Z. Cui, D. Chen, X. Pang, Q. Zhang, F. Shao, H. Dong, L. Yu and L. Dong, *Renewable Energy*, 2021, **163**, 375–385.
75 C. Zhang, K. B. Hatzell, M. Boota, B. Dyatkin, M. Beidaghi, D. Long, W. Qiao, E. C. Kumbur and Y. Gogotsi, *Carbon*, 2014, **77**, 155–164.
76 A. Ganesan and M. M. Shaijumon, *Microporous Mesoporous Mater.*, 2016, **220**, 21–27.
77 G. Singh, K. S. Lakhi, K. Ramadass, S. Kim, D. Stockdale and A. Vinu, *Microporous Mesoporous Mater.*, 2018, **271**, 23–32.
78 P. Hao, Z. Zhao, Y. Leng, J. Tian, Y. Sang, R. I. Boughton, C. Wong, H. Liu and B. Yang, *Nano Energy*, 2015, **15**, 9–23.
79 F. Kapteijn, J. Moulijn, S. Matzner and H.-P. Boehm, *Carbon*, 1999, **37**, 1143–1150.

80 B. Sun, Y. Yuan, H. Li, X. Li, C. Zhang, F. Guo, X. Liu, K. Wang and X. Zhao, *Chem. Eng. J.*, 2019, **371**, 55–63.
81 N. A. Rashidi, S. Yusup, M. M. Ahmad, N. M. Mohamed and B. H. Hameed, *APCBEE Proc.*, 2012, **3**, 84–92.
82 M. L. Martinez, M. M. Torres, C. A. Guzman and D. Maestri, *Ind. Crops Prod.*, 2006, **23**, 23–28.
83 C. Arnas, C. Dominique, P. Roubin, C. Martin, C. Laffon, P. Parent, C. Brosset and B. Pegourie, *J. Nucl. Mater.*, 2005, **337**, 69–73.
84 A. Sahu, S. Sen and S. C. Mishra, *Diamond Relat. Mater.*, 2020, **108**, 107931.
85 A. Wang, K. Sun, R. Xu, Y. Sun and J. Jiang, *J. Cleaner Prod.*, 2021, **283**, 125385.
86 T. Liang, C. Chen, X. Li and J. Zhang, *Langmuir*, 2016, **32**, 8042–8049.
87 H. B. M. Emrooz, M. Maleki and A. Rahmani, *J. Taiwan Inst. Chem. Eng.*, 2018, **91**, 281–290.
88 J. Deng, T. Xiong, F. Xu, M. Li, C. Han, Y. Gong, H. Wang and Y. Wang, *Green Chem.*, 2015, **17**, 4053–4060.
89 J. Hao, Y. Wang, C. Chi, J. Wang, Q. Guo, Y. Yang, Y. Li, X. Liu and J. Zhao, *Sustainable Energy Fuels*, 2018, **2**, 2358–2365.
90 J. Liu, L. Zhang, C. Yang and S. Tao, *J. Mater. Chem. A*, 2019, **7**, 21168–21175.
91 D. B. Altuntaş, V. Nevruzoğlu, M. Dokumacı and Ş. Cam, *Carbon Letters*, 2020, **30**, 307–313.
92 M. O. Prakash, G. Raghavendra, S. Ojha and M. Panchal, *Mater. Today: Proc.*, 2021, **39**, 1476–1481.
93 C. Wang, H. Wang, B. Dang, Z. Wang, X. Shen, C. Li and Q. Sun, *Renewable Energy*, 2020, **156**, 370–376.
94 D. Park, Y. Ju, J.-H. Kim, H. Ahn and C.-H. Lee, *Sep. Purif. Technol.*, 2019, **223**, 63–80.
95 V. M. Matsis and H. P. Grigoropoulou, *Chem. Eng. Sci.*, 2008, **63**, 609–621.
96 A. Ansón, S. M. Kuznicki, T. Kuznicki, T. Haastrup, Y. Wang, C. C. Lin, J. A. Sawada, E. M. Eyring and D. Hunter, *Microporous Mesoporous Mater.*, 2008, **109**, 577–580.
97 Y.-J. Park, S.-J. Lee, J.-H. Moon, D.-K. Choi and C.-H. Lee, *J. Chem. Eng. Data*, 2006, **51**, 1001–1008.
98 Y. Zhou, L. Wei, J. Yang, Y. Sun and L. Zhou, *J. Chem. Eng. Data*, 2005, **50**, 1068–1072.
99 M. Andrade, S. C. Rodrigues and A. Mendes, *Microporous Mesoporous Mater.*, 2020, **296**, 109989.
100 J. V. Nabais, P. Carrott, M. R. Carrott, A. Padre-Eterno, J. Menéndez, A. Dominguez and A. Ortiz, *Carbon*, 2006, **44**, 1158–1165.
101 R. R. Pawar, H. A. Patel, G. Sethia and H. C. Bajaj, *Appl. Clay Sci.*, 2009, **46**, 109–113.
102 D. Saha and M. J. Kienbaum, *Microporous Mesoporous Mater.*, 2019, **287**, 29–55.
103 B. H. Kim, B. R. Kim and Y. G. Seo, *Adsorption*, 2005, **11**, 207–212.
104 J. J. Manyà, B. González, M. Azuara and G. Arner, *Chem. Eng. J.*, 2018, **345**, 631–639.
105 C. Reid, I. O'koy and K. Thomas, *Langmuir*, 1998, **14**, 2415–2425.
106 P. Ehrburger, O. Mahajan and P. Walker Jr, *J. Colloid Interface Sci.*, 1976, **57**, 233–239.
107 N. Kobayashi, T. Enoki, C. Ishii, K. Kaneko and M. Endo, *J. Chem. Phys.*, 1998, **109**, 1983–1990.
108 S. M. Wilson and F. H. Tezel, *Sep. Purif. Technol.*, 2021, **258**, 117659.
109 F. Raganati, M. Alfe, V. Gargiulo, R. Chirone and P. Ammendola, *Chem. Eng. Res. Des.*, 2018, **134**, 540–552.
110 H. Mashhadimoslem, M. Vafaeinia, M. Safarzadeh, A. Ghaemi, F. Fathalian and A. Maleki, *Ind. Eng. Chem. Res.*, 2021, **60**, 13950–13966.
111 H. M. Yi, S. Weiruo, B. Maruti, W. Jinqu and G. W. Miller, *Sep. Technol.*, 1991, **1**, 90–98.
112 S. Rutherford and J. Coons, *J. Colloid Interface Sci.*, 2005, **284**, 432–439.
113 Y.-S. Bae and C.-H. Lee, *Carbon*, 2005, **43**, 95–107.
114 R. Bazan, M. Bastos-Neto, A. Moeller, F. Dreisbach and R. Staudt, *Adsorption*, 2011, **17**, 371–383.